STATE OF THE CLIMATE IN 2016

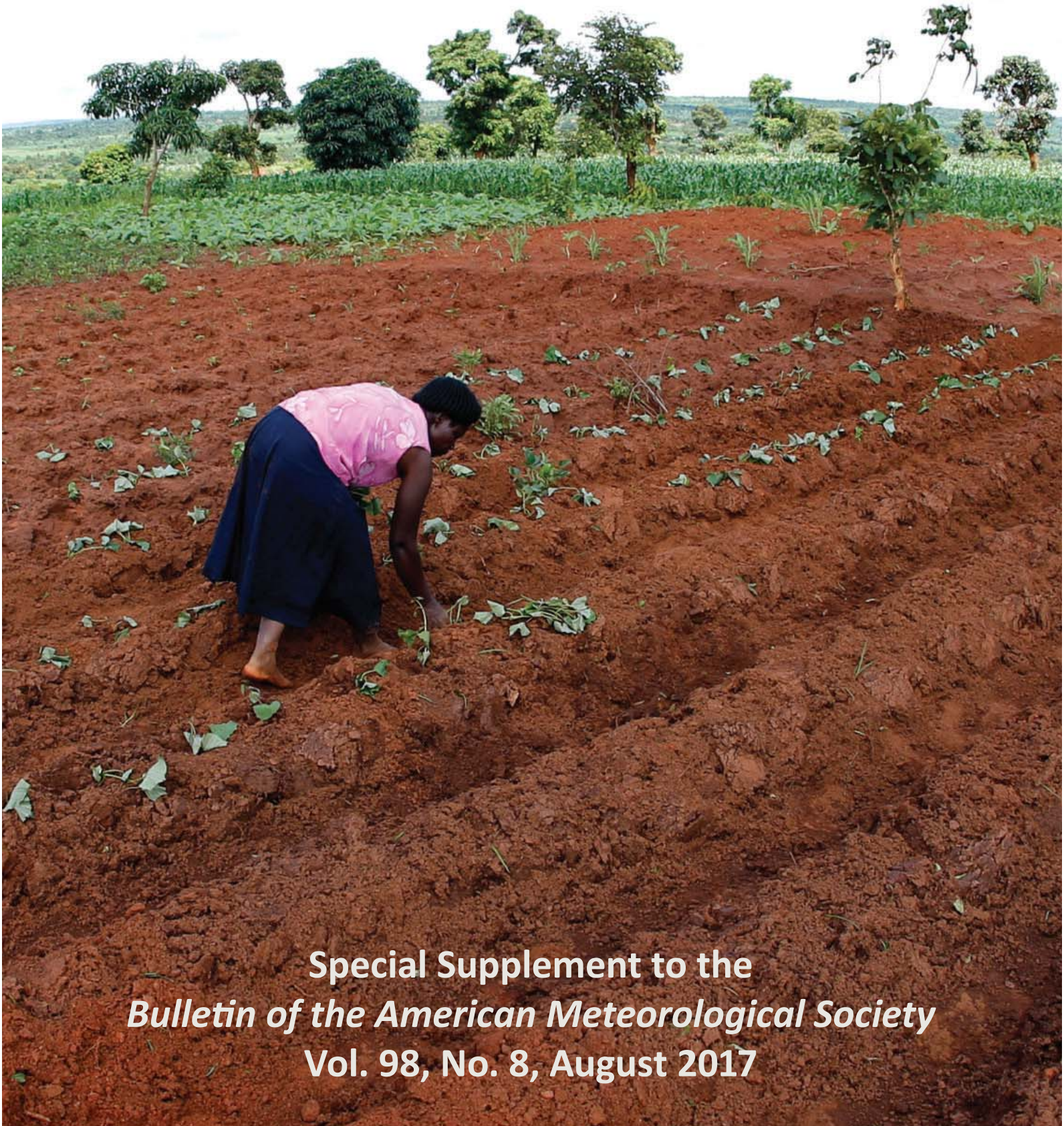

Special Supplement to the
Bulletin of the American Meteorological Society
Vol. 98, No. 8, August 2017

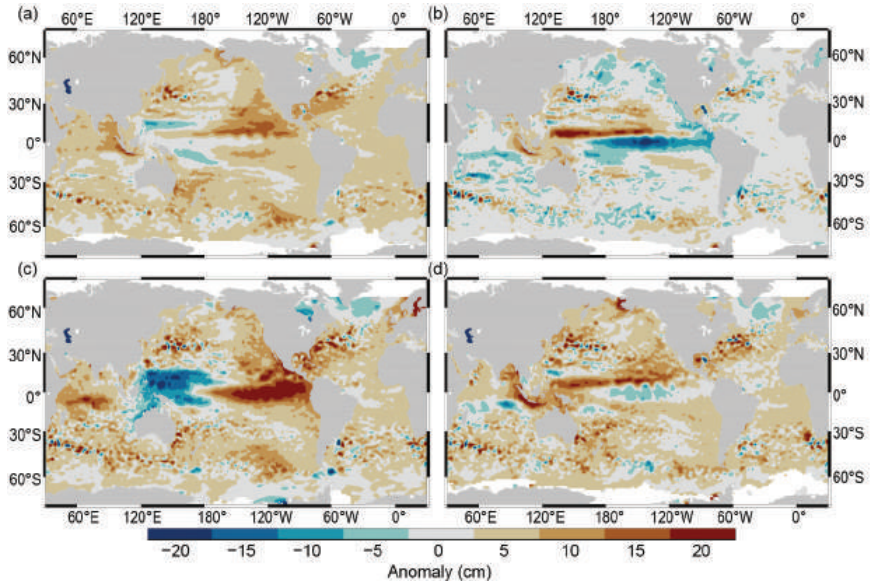

Fig. 3.16. (a) Annual average sea level anomaly during 2016 relative to the average sea level at each location during 1993–2016. (b) Average 2016 sea level anomaly minus 2015. (c) Average sea level anomaly during Dec 2015–Feb 2016 (DJF) relative to the DJF average during 1993–2016. (d) As in (c), but for Sep–Nov 2016. Anomalies are in cm. Altimetry data were obtained from the gridded, multimission product maintained by CMEMS.

densities in the deep Labrador Sea (Rahmstorf et al. 2015; Robson et al. 2016).

Global and regional mean sea level change affects coastal communities by changing the frequency of positive sea level extremes that cause flooding and erosion. Infrastructure within coastal communities is currently exposed to "nuisance" (associated with minor impacts) tidal flooding at a median height of about 0.5 m above mean higher high water (MHHW) tidal datum (Sweet et al. 2014), which is approximated as the long-term average of daily highest water levels. High-frequency measurements by a global set of tide gauges find that the median of the top 1% of observed daily maximum heights (three to four days per year on average) is also about 0.5 m above MHHW (Fig. 3.17a). During 2016, multiple regions experienced greater-than-average numbers of such sea level extremes: the U.S. East Coast, the central South Pacific, southern Australia, and the tropical Indian Ocean (Fig. 3.17b). The U.S. West Coast did not experience a greater number of sea level extremes despite substantially elevated mean sea levels in the region (Fig. 3.16a). Relative to 2015, spatially coherent increases in sea level extremes occurred over the U.S. northeast coast, Hawaii, portions of East Asia, and southern Australia (Fig. 3.17c).

Two factors can lead to increased numbers of positive sea level extremes: elevated background mean sea level and increased storminess (e.g., Sweet and Park 2014). High-pass filtering the tide gauge observations with a cut-off period of 30 days and then repeating the calculations in Fig. 3.17 reveals the contribution of synoptic timescales (i.e., storminess) to sea level extremes in the tide gauge records (not shown). The filtering exercise suggests that increased storminess mostly accounts for the increased number of 2016 extremes along the U.S. northeast and East Asian coastlines and partially accounts for the increase in southern Australia and the tropical Indian Ocean. This leaves background sea level change as the dominant contribution to elevated numbers of sea level extremes in the southeast U.S., Hawaii, and central South Pacific. Along the southeast U.S. coastline, the increase may be related to the hypothesized slowdown of the Florida Current and Gulf Stream during recent decades (Ezer et al. 2013; Sweet et al. 2016), which would tend to raise coastal sea level in the region. Increased numbers of extremes in the central South Pacific most likely relate to multidecadal regional sea level trends (Fig. 3.15b), because the annual anomaly in the region is generally small (Fig. 3.16a) and the number of extremes decreases relative to 2015 (Fig. 3.17c). The opposite is true for Hawaii, where the multidecadal trend is small (Fig. 3.15b), but the annual anomaly is large (Fig. 3.16a) due to Rossby waves emanating from the eastern boundary during mid- to late 2016 in response to ENSO forcing along the equator.

g. *Surface currents*—R. Lumpkin, G. Goni, and K. Dohan

This section describes ocean surface current changes, transports derived from ocean surface currents, and features such as rings inferred from surface currents. Surface currents are obtained from in situ (global array of drogued drifters and moorings) and satellite (altimetry, wind stress, and SST) observations. Transports are derived from a combination of sea height anomaly (from altimetry) and climatological hydrography. See Lumpkin et al. (2012) for details of the datasets used and calculations performed. Anomalies are calculated with respect to the time period 1992–2007. Annually averaged zonal current anomalies and changes in anomalies from the previous year are shown in Fig. 3.18, while seasonal averages are shown in Fig. 3.19. These anomalies are discussed below for individual ocean basins.

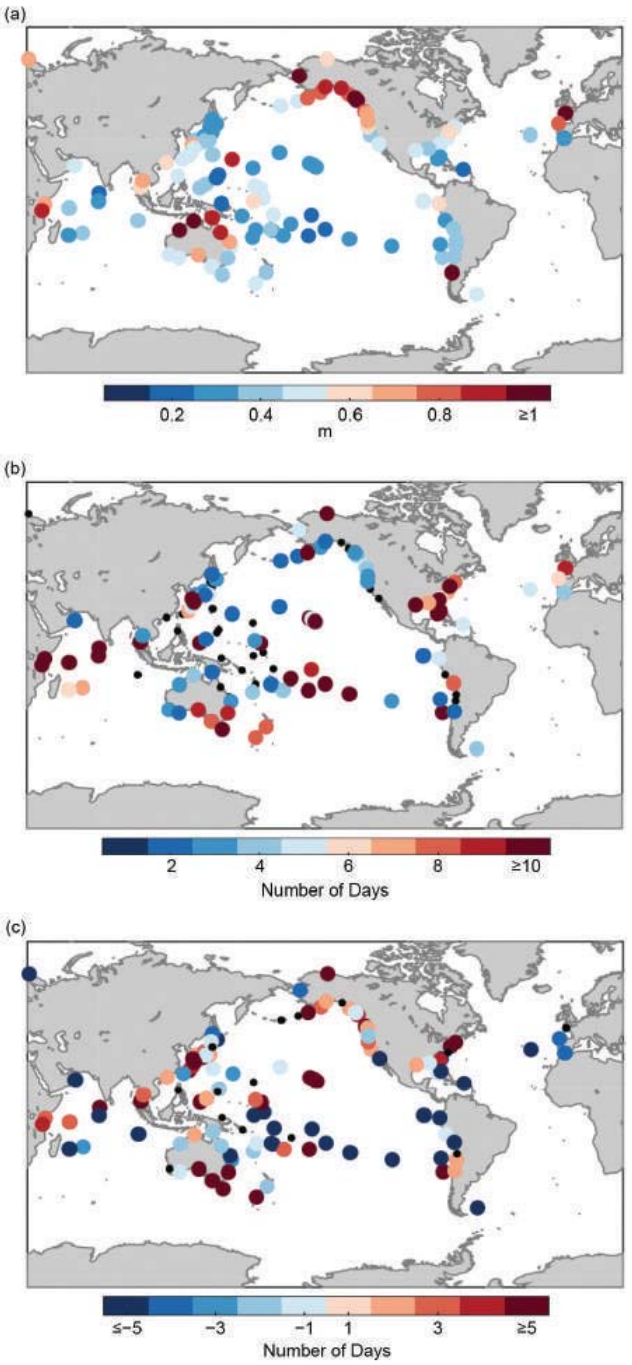

Fig. 3.17. (a) Thresholds defining an extreme sea level anomaly (m) for each station in the presnt analysis. 1% of daily maximum water levels at each station reach heights indicated by the colors in the figure. Units are meters above mean higher high water (MHHW) calculated over 1996–2015. (b) Number of daily maximum water levels during 2016 above the thresholds in (a). Small, black circles in (b) and (c) indicate a value of zero. (c) As in (b), but for 2016 minus 2015. Daily maximum water levels were calculated from hourly tide gauge observations obtained from the University of Hawaii Sea Level Center Fast Delivery database. Only records with at least 80% completeness during 1996–2015 and 80% completeness during 2016 were analyzed.

l) Pacific Ocean

Westward anomalies across the equatorial Pacific, associated with the 2016 La Niña, dominated annual mean current anomalies in the Pacific basin (Fig. 3.18a). These anomalies had an annually averaged value of 12–16 cm s^{-1} between 1°S and 6°N. Farther north, a narrow band of eastward anomalies peaked at 15–17 cm s^{-1} between 9° and 10.5°N, on the northern flank of the climatological North Equatorial Countercurrent (NECC), associated with a northward displacement of that current. Because 2015 was characterized by a reversal of these patterns, that is, intense eastward equatorial anomalies during the 2015/16 El Niño and westward anomalies in a weakened NECC, the 2016 minus 2015 tendencies (Fig. 3.18b) are a magnified version of the 2016 anomalies.

The year 2016 began (Fig. 3.19) with El Niño-related eastward anomalies exceeding 20 cm s^{-1} between 2°S and 5°N in the central basin, with peak anomalies of 40 cm s^{-1} at 3°N. These anomalies had reversed by February, with westward anomalies of 20–30 cm s^{-1} between the equator and 2°N. By March, these anomalies were quite dramatic in the eastern half of the basin, with peak values of 50 cm s^{-1} westward between 100°W and 155°W. As a consequence, the westward flow there increased from 75 cm s^{-1} (the climatological March value) to ~130 cm s^{-1}. Strong westward anomalies persisted and spread westward

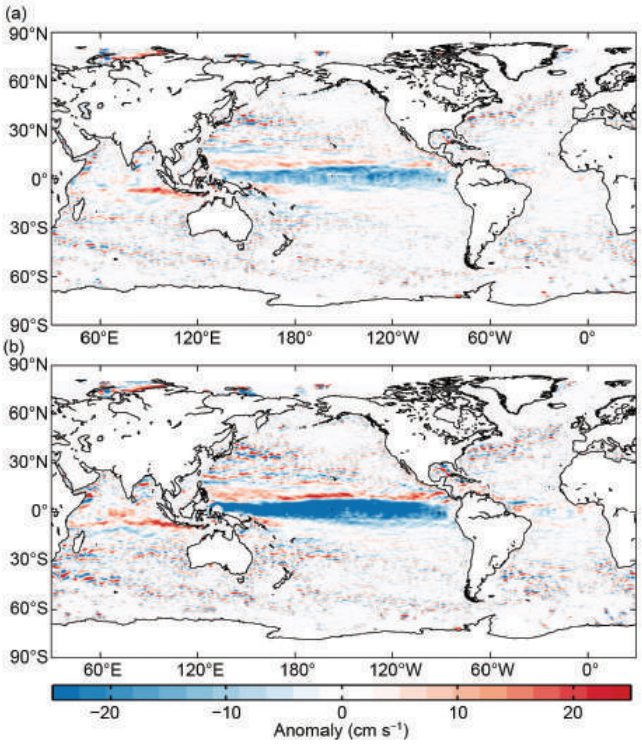

Fig. 3.18. Annually averaged geostrophic zonal current anomalies (cm s^{-1}) for (a) 2016 and (b) 2016 minus 2015 derived from a synthesis of drifters, altimetry, and winds.

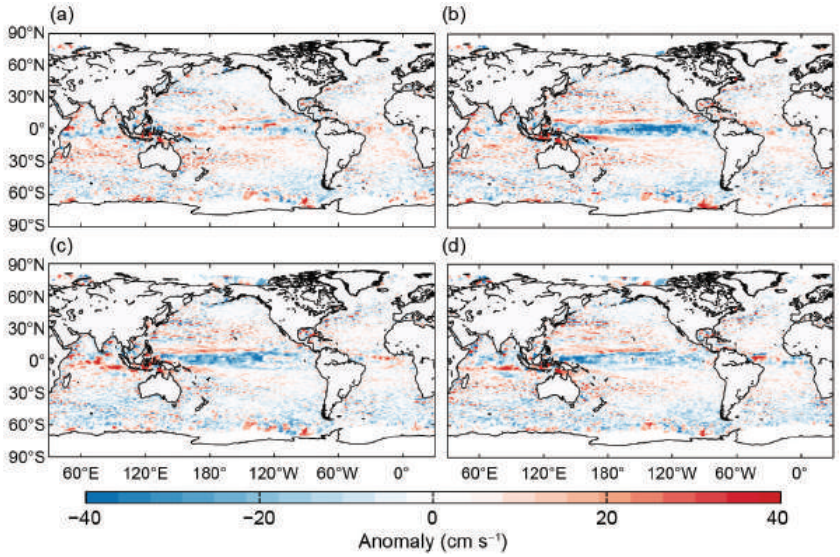

Fig. 3.19. Seasonally averaged zonal geostrophic anomalies (cm s^{-1}) with respect to seasonal climatology, for (a) Dec 2015–Feb 2016, (b) Mar–May 2016, (c) Jun–Aug 2016, and (d) Sep–Nov 2016.

through April and May, by which point they were seen across the entire Pacific basin. These westward anomalies acted to reverse the sea level anomaly pattern across the basin (Figs. 3.16c,d) and erase the >2°C SST anomalies in the eastern tropical Pacific (see Figs. 3.2a–c). In June, these anomalies began to weaken in the eastern half of the basin, and in July, they weakened across the basin when peak anomalies of ~25 cm s^{-1} were at 3°–4°N. These westward anomalies continued to weaken throughout the rest of the year; in December, they averaged 10–15 cm s^{-1} at 4°–6°N.

As noted in earlier *State of the Climate* reports (e.g., Dohan et al. 2015), the Kuroshio was shifted anomalously northward in 2010–14, although this shift diminished in 2014. During 2015 and 2016, the Kuroshio was close to its climatological latitude.

Equatorial Pacific surface current anomalies advect surface waters across the basin, resulting in SST anomalies. These surface current anomalies typically lead SST anomalies by several months, with a magnitude that scales with the SST anomaly magnitude. SST anomalies typically continue to rise until the currents return to normal conditions. Thus, current anomalies in this region are a valuable predictor of the evolution of SST anomalies and their related climate impacts. This leading nature can be seen in the first principal empirical orthogonal function (EOF) of surface current anomaly (SC) and separately the first EOF of SST anomaly (SST) in the tropical Pacific basin (Fig. 3.20). The maximum lagged correlation between SC and SST is R = 0.66 for 1993–2016, with SC leading SST by 81 days. The year began with positive SST and SC anomalies. SC anomalies sharply reversed in January, dropping to a minimum EOF amplitude value of –2.9 standard deviations in April—the smallest value in the record—and remaining negative throughout the year. These westward SC anomalies resulted in a lowering of SST anomalies, although with such strong positive SST anomalies at the start of the year, the SST EOF amplitude remained positive for most of 2016.

2) Indian Ocean

The annually averaged near-equatorial current in the Indian Ocean basin is eastward, reflecting the dominance of the Southwest Monsoon Current in the annual average. During 2016, the mean current near the equator was up to 20 cm s^{-1} faster (anomalous eastward current) in the eastern half of the basin, with the largest anomalies at 6°–8°S. Because these anomalies were not seen in 2015, they appear in both the 2016 annual average (Fig. 3.18a) and the 2016 minus 2015 tendencies (Fig. 3.18b). An examination of the month-by-month development of these anomalies reveal that they reflect a much-stronger-than-average Southwest Monsoon Current in the second half of the year. The year 2016 began with >20 cm s^{-1} westward anomalies from 5°S to 1°N in the central Indian Ocean, which weakened in February and March and were largely absent by April. In May, very strong (25 cm s^{-1}) eastward equatorial anomalies developed across the

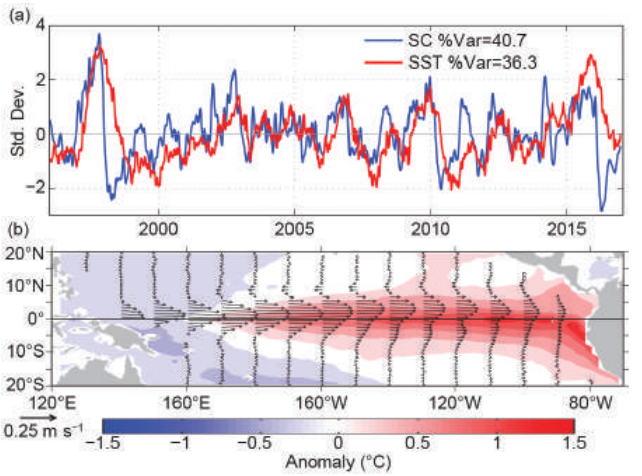

Fig. 3.20. Principal empirical orthogonal functions (EOF) of surface current (SC; m s^{-1}) and of SST anomaly (°C) variations in the tropical Pacific from the OSCAR model (Bonjean and Lagerloef 2002; www.esr.org/enso_index.html). (a) Amplitude time series of the EOFs normalized by their respective standard deviations. (b) Spatial structures of the EOFs.

basin. Through June and July, these anomalies intensified and propagated east and south, as the current is deflected off the equator by the presence of the Malaysian coast. The anomalies weakened slightly in August, then persisted at approximately the same strength (30–35 cm s^{-1} eastward in the region 6°–8°S, 80°–100°E) through the end of 2016.

The Agulhas Current transport is a key indicator of Indian–Atlantic Ocean interbasin water exchanges. The annual mean transport of the Agulhas Current decreased over the period 2013–15, from 56 Sv (1 Sv ≡ 10^6 m^3 s^{-1}) in 2013 to 50 Sv in 2015 (www.aoml.noaa.gov/phod/altimetry/cvar). In 2016, the Agulhas Current had an annual average transport of 54 Sv, exceeding the long-term mean of 50 Sv. These changes are larger than the ~3 Sv standard deviation of the individual yearly estimates.

3) Atlantic Ocean

Annual mean anomalies in the Atlantic Ocean (Fig. 3.18a) indicate an 8–10 cm s^{-1} strengthening of the eastward NECC and comparable weakening of the westward northern South Equatorial Current (nSEC) at 2°–5°N, 15°–40°W. Elsewhere, conditions were near climatology. Because anomalies were weaker in 2015, the 2016 minus 2015 map (Fig. 3.18b) closely resembles the 2016 map. Looking at the month-to-month development of anomalies, large-scale conditions were close to climatology until May, when eastward anomalies began developing across the equatorial band, indicating a slowing of the westward nSEC. By June, these anomalies exceeded 20 cm s^{-1} at 1°–3°N, 0°–30°W. They then weakened through July and August, when eastward anomalies began developing to the north, in the latitude band of the NECC. These anomalies, which dominated the annual average, intensified through September–November in the western NECC and were still present at the end of the year. Averaged over the last four months of the year, eastward anomalies peaked at 30 cm s^{-1} at 4°N, 30°–45°W. Weaker westward anomalies centered at 6°N in the same longitude band indicate that the NECC was not only stronger, but also shifted somewhat south of its climatological position.

The mean position of the Gulf Stream extension shifted north by approximately 0.5° latitude in 2016 relative to climatological values (see Sidebar 3.1 for related impacts), while the Loop Current did not extend as fully into the Gulf of Mexico on average in 2016 as it had in the previous two years.

In the southwest Atlantic Ocean, the Brazil Current carries waters from subtropical to subpolar regions mainly in the form of large anticyclonic rings (Lentini et al. 2006). The separation of the Brazil Current front from the continental shelf break continued to exhibit annual periodicity (www.aoml.noaa.gov/phod/altimetry/cvar), which is mainly driven by wind stress curl variations and the transport of this current. During 1993–2005, the annual mean separation of the front shifted southward in response to a long-term warming in South Atlantic temperatures (cf. Lumpkin and Garzoli 2011; Goni et al. 2011). Since 2005, the location of the front has not exhibited interannual trends. The year 2016 was an anomalous one in which the front was persistently shifted north of its long-term mean position—something not seen since 1994. It remains to be seen if this represents a transient or more sustained reversal of the long-term shift of the confluence to the south.

h. Meridional overturning and oceanic heat transport circulation observations in the North Atlantic Ocean—M. O. Baringer, D. A. Smeed, J. Willis, M. Lankhorst, W. R. Hobbs, S. Dong, G. McCarthy, D. Rayner, W. E. Johns, G. Goni, and U. Send

This section describes the AMOC and the Atlantic meridional heat transport (AMHT), determined by the large-scale ocean circulation wherein northward moving upper layer waters are transformed into deep waters that return southward, redistributing heat, fresh water, carbon, and nutrients. Large variations in meridional heat transport are associated with strong MOC anomalies (e.g., correlations of 0.94, Johns et al. 2011) and northwesterly wind anomalies while monthly variability is more closely linked to the spatial structure associated with the North Atlantic oscillation (NAO; e.g., Moat et al. 2016). Observed cold North Atlantic sea surface temperatures were consistent with the decadal decrease in MOC transport at 26°N (e.g., Baringer et al. 2016). These large-scale ocean anomalies can subsequently impact European weather (e.g., Duchez et al. 2016). Many climate, weather, and ecosystem changes covary with changes in the AMOC (e.g., Srokosz and Bryden 2015; Carton et al. 2014; Srokosz et al. 2012).

The AMOC is computed as the maximum of the vertical accumulation of the horizontally integrated velocity across a zonal-vertical section (i.e., the maximum transport that occurs in either the upper or lower layer before the circulation starts to change direction again). The AMHT involves the covariability of temperature and velocity and is only meaningful as a flux (and hence, independent of the absolute temperature scale used) when the total mass transport can be accounted for (i.e., sums to zero). Observing systems can measure both temperature and velocity, usually with tradeoffs in system design